Surface & Coatings Technology 476 (2024) 130184

Contents lists available at ScienceDirect

Surface & Coatings Technology

journal homepage: www.elsevier.com/locate/surfcoat

Full Length Article

Screening of fluoride-free PEO coatings on cast Mg3Zn0.4Ca alloy for orthopaedic implants

Lara Moreno [a,*], Marta Mohedano [a], Raul Arrabal [a], Endzhe Matykina [a,b]

[a] Departamento de Ingeniería Química y de Materiales, Facultad de Ciencias Químicas, Universidad Complutense de Madrid, 28040 Madrid, Spain
[b] Unidad Asociada al ICTP, IQM (CSIC), Grupo de Síntesis Orgánica y Bioevaluación, Instituto Pluridisciplinar (UCM), Paseo de Juan XXIII, 1, Madrid 28040, Spain

ARTICLE INFO

Keywords:
Magnesium
Plasma electrolytic oxidation
Degradation rate
Coating
Implant

ABSTRACT

In order to improve the corrosion behaviour of Mg3Zn0.4Ca alloy, fluorine-free PEO coatings, developed at different treatment times using a novel transparent electrolyte and a conventional suspension electrolyte, were compared. The surface morphology and chemical composition of the PEO coatings were evaluated by scanning electron microscopy, transmission electron microscopy and X-ray diffraction. The corrosion behaviour of the PEO coatings was carried out by potentiodynamic polarization, electrochemical impedance spectroscopy and hydrogen evolution test in modified α-MEM solution. The coatings formed in both electrolytes showed very similar morphologies and compositions that were independent of the nature of the electrolyte. At short immersion times, all PEO coatings showed an improvement in corrosion resistance by PDP measurements, while by EIS measurements only the coatings at short treatment times showed a significant improvement. After >24 h of immersion, the PEO coating formed in transparent electrolyte suffered a drastic acceleration of the degradation rate that exceeded that of the uncoated substrate. The acceleration was attributed to the presence of a crack at the PEO/substrate interface, and the formation of ZnO from the oxidation of Zn-rich secondary phases of the Mg3Zn0.4Ca alloy. The PEO coating formed in the suspended electrolyte on the Mg3Zn0.4Ca alloy showed great corrosion protection, which was attributed to the precipitation of hydroxyapatite that remains trapped in the pores and cracks of the PEO coatings by the hydrolysed silica, impeding the progress of corrosive species.

1. Introduction

Plasma electrolytic oxidation (PEO) is an anodizing process carried out at high voltage in an alkaline electrolyte. PEO process is a promising strategy for generating a variety of bioactive coatings with a wide range of compositions, microstructures, porosity and roughness achievable though control of the PEO process parameters and electrolyte composition [1,2]. During the PEO process, the formation of the coating depends on the interaction of species from the electrolyte and substrate species [3–5].

The high fluorine content (e.g. 8 g/L) in the electrolyte leads to a great improvement of the corrosion resistance of Mg alloys due to the formation of thick coatings, in the range of 35–40 μm, simultaneously improving the cell adhesion and proliferation [6]. Nevertheless, some studies pinpointed low biocompatibility of fluoride-containing coatings with endothelial cells due to the cells' limited tolerance to the released fluoride. In order to avoid premature cell death while maintaining the protective properties of the coatings, PEO coatings were developed on a cast Mg3Zn0.4Ca alloy with reduced fluoride content in the electrolyte (3 g/L) where thicknesses between 10–18 μm were obtained. However, the corrosion protection of these coatings was lower compared to the substrate, which was associated with the presence of Zn-rich intermetallics embedded in the coating and the easy permeability of the coatings due to insufficient amount of MgF_2 in the barrier layer [7].

To avoid fluoride presence in the coating, Ca-, P- and Si-based electrolytes were developed in order to promote the formation of compounds such as hydroxyapatite improving the corrosion resistance of Mg alloys and enhancing the cell adhesion and proliferation which is particularly important for biomedical applications [6,8]. Furthermore, the combination of Ca and P salts in PEO electrolyte results in suspension electrolytes due to precipitation of calcium phosphates, which require higher maintenance due to the particle agglomeration. For this reason, the addition of organic complexing additives such as ethylenediaminetetraacetic acid (EDTA) is required in order to stabilize Ca^{2+} in the solution and avoid formation of particles [9,10].

Most of the published works that attempted to improve the corrosion

* Corresponding author.
E-mail address: laramo01@ucm.es (L. Moreno).

https://doi.org/10.1016/j.surfcoat.2023.130184
Received 19 July 2023; Received in revised form 13 September 2023; Accepted 7 November 2023
Available online 17 November 2023

resistance of Mg-Zn-Ca alloys using bioactive PEO coatings employed Ca—P, Ca-P-Si or Si-based suspension electrolytes (some with addition of fluoride species) [11–13]. Such coatings were reported to improve the corrosion performance compared to the bare substrates [14–16]. However, the corrosion performance of these systems is typically evaluated by electrochemical or immersion tests without pH control (i.e. without maintaining pH 7.4) during the test. The latter has been recently reported to have an important effect on the corrosion rate of Mg-Zn-Ca alloys [7].

The present work is focused on the comparative study of the PEO coatings formed on Mg3Zn0.4Ca alloy in a suspension electrolyte and a true solution electrolyte, both specially designed to be F-free and contain bioactive Ca, Si and P species. The study evaluates the coating growth kinetics, morphology and composition. The corrosion behaviour of the coated systems is evaluated in modified α-MEM solution employing constant pH control during the immersion tests in order to emulate *in vivo* implant degradation conditions. The long-term (120h) immersion results are compared with a short-term (1h) screening by means of electrochemical tests in an attempt to propose a reliable protocol of coating selection for subsequent *in vitro* biological studies.

2. Materials and methods

2.1. Materials

Mg3Zn0.4Ca cast ingot determined by Arc Spark analysis is constituted by (wt.%): 3.14 Zn, 0.4 Ca, 0.002 Cu, 0.012 Fe, balanced Mg. The alloy was supplied by the Institute of Surface Science (Helmholtz-Zentrum Hereon, Geesthacht, Germany). The sample was prepared by grinding to P1200 grit size SiC papers, rinsed in isopropyl alcohol and dried in warm air.

2.2. PEO treatment

Alternating current (AC) voltage-controlled power supply (EAC-S2000, ET Systems electronic) was used for PEO treatment in 2 L double jacket thermostat glass cell. The Mg3Zn0.4Ca alloy was used as work electrode and stainless steel mesh (AISI 316 of Ø15cm) as counter electrode. The coating was formed on the entire specimen, with the electrical contact provided through a threaded insulated brass rod. The root-mean-square (rms) voltage and current responses were controlled electronically, with a sampling time of 0.1 s, employing a Keithley KUSB-3116 data acquisition card (16 bit, 500 Ks/s) and Labview program (National Instruments). Instantaneous voltage and current values were monitored using a 2-channel Tektronix TDS 2012B oscilloscope at 100 MHz sampling rate.

The transparent electrolyte was designed based on Ca, P and Si species by adjusting the molar ratio of Ca and EDTA species in order to avoid suspended particles, such as $Ca_3(PO_4)_2$, and achieve sustainable microdischarges and uniform coatings. This electrolyte was compared with an electrolyte in suspension. The composition of both electrolytes and the electrical parameters of the process are presented in the Table 1. After PEO process, the samples were rinsed in deionized water dried with warm air.

2.3. Surface characterization

A JEOL JSM-6400 scanning electron microscope equipped with an X-ray energy dispersive system (EDS) was used to determine the composition and morphology of the coated samples. All samples were prepared by grinding from P120 to P1200 grit of SiC abrasive papers and polishing from 3 to 1 μm using diamond paste.

X-ray diffraction (XRD) patterns and X'PertHighScore software and ICDDD PDF4+ database of the phase components of the coatings were measured with Philips X'Pert diffractometer operated in Bragg-Brentano geometry (CuKα = 0.154056 nm, 450 kV, 400 mA, scan rate 0.04°/s, range 2Θ: 10–80°).

Table 1
Composition and PEO process parameters of electrolytes.

Composition	Electrolyte (g/L)	
	PEO-T Transparent	PEO-S Suspension
$Na_3PO_4{\cdot}12H_2O$	10	10
$Na_2SiO_3{\cdot}5H_2O$	10	9
KOH	8	1
$CaH_7C_3PO_6$	2	–
CaO	–	2.9
Na_2EDTA	3.67	–
σ(mS·cm^2)	40.1	24.6
pH	12.7	12.9
Parameters of PEO		
Waveform	Square	
Voltage (V)	+350/−50	
Current density (mA/cm^2)	100	
Duty cycle (%)	50	
Frequency (Hz)	50	
Time (s)	300/600/900	

The roughness parameters S_a (arithmetic mean area height) and S_{10z} (ten point height) were evaluated using a 3D optical focus variation profilometer (InfiniteFocus SL, ALICONA). The values presented are the average of 3 measurements over a length of 2.8 mm.

The coating thickness was measured with the Fischer ISOSCOPE FMP10 portable eddy current meter using an average of ten measurements and subsequently confirmed with cross-sectional SEM. The pore population density and pore size of the coatings were estimated using ImageJ software. Image analysis of the coating surface was carried out using three SEM micrographs taken at arbitrary locations.

The barrier layer of the PEO-S coating at 300 s was analysed by TEM using JEOL JEM 2100 instrument operated at 200 kV. The sample was assembled in a sandwich structure (diameter 3 mm) and subsequently thinned until <0.1 mm thick. After that, the specimen was prepared by ion milling in a 691 GATAN PIPs system with a small incident angle until perforation.

2.4. Corrosion testing

The corrosion behaviour of the specimens was analysed by electrochemical and hydrogen evolution tests in a modified α-MEM solution (Minimum Essential Medium Eagle-alpha, free from organic additives) prepared in the laboratory, consisting of 6.8 g/L NaCl, 2.2 g/L $NaHCO_3$, 0.4 g/L KCl, 0.12 g/L Na_2HPO_4, 0.09 g/L $MgSO_4$, 0.2 g/L $CaCl_2$ at 37 °C.

2.4.1. Electrochemical measurements

A GillAC potentiostat (ACM Instruments) was used to analyse the corrosion behaviour of electrochemical tests in modified α-MEM after 1 h of immersion. A standard three electrode cell, an Ag/AgCl-3 M as reference electrode, platinum as counter electrode and PEO-coated specimens with an exposed area of 1 cm^2 as working electrode, were used to monitor the evolution of the electrochemical data.

Potentiodynamic polarization curves were performed at a scanning rate of 0.3 mV/s with potential sweep from −200 mV to +1000 mV (vs. OCP), and a current density limit of 5 mA/cm^2. From the analysis of cathodic and anodic Tafel slopes, the corrosion current density and corrosion potential were obtained. Electrochemical impedance spectroscopy (EIS) measurements were carried out in the frequency range from 100 kHz to 10 mHz at the open circuit potential, with a sinusoidal perturbation of 10 mV amplitude. The acquired EIS data were fitted by ZView software and a good fit was ensured through keeping the square of the standard deviation between the original and the calculated spectra <0.01 and the weighted sum of squares (proportional to the average percentage error between the original data points and the

calculated values) <0.1.

2.4.2. Hydrogen evolution test

Hydrogen evolution measurements for bulk material and PEO-coated specimens were carried out during 5 days immersion. The specimens were placed in 25 mL burettes into a plastic chamber of 12 L connected with the 9 L deposit. The pH of the physiological solution was continuously adjusted to 7.4 by a flow of CO_2 regulated by a switch coupled to a pH-sensor. Each material was tested by triplicate to obtain the average value. The total surface area of the immersed specimens was ~18 cm^2.

3. Results and discussion

3.1. Electrical response of PEO treatment

Fig. 1 (a) shows the evolution of the root mean square values of voltage and current density (U_{rms}, i_{rms}) during PEO treatment in transparent and suspension (PEO-T and PEO-S, respectively) electrolytes on Mg3Zn0.4Ca alloy. For both electrolytes, a linear voltage increase is observed during the 60 s ramp with a slight change of slope at ~35 s (230 V) that occurs when the limiting current density of 100 $mA{\cdot}cm^{-2}$ is reached. A second inflexion occurs at ~50 s (~200 V) corresponding to visual initiation of the plasma microdischarges indicating a change in the oxide layer growth kinetics. In PEO-T electrolyte, the microdischarges are distributed across the surface of the sample, while in PEO-S visual examination of the discharge is not possible because the addition of practically insoluble CaO resulted in opacity of the electrolyte. After that point, the voltage gradually reaches an approximately constant value of ~235 V in PEO-S and ~229 V in PEO-T. This slight difference indicates that impedance during the process is greater for PEO-S, which may be attributed to the greater compactness of the coating material.

The calculated apparent specific energy consumption for PEO-coated samples are illustrated in Fig. 1 (b). The calculation was done according to the formula.

$$E\left(W{\cdot}s{\cdot}cm^{-2}\right) = \int_{t0}^{tf} \left(\text{current density}\left(A{\cdot}cm^{-2}\right) \times \text{Voltage}\,(V)\right)$$

where $t_0 = 0$ s and t_f is the duration of the PEO coating process. The specific energy consumption is obtained by dividing the energy by the coating thickness and adjusting the units to $kW{\cdot}h{\cdot}m^{-2}{\cdot}\mu m^{-1}$.

For both systems, the results indicated an increase of energy consumption from <0.25 $kW{\cdot}h{\cdot}m^{-2}{\cdot}\mu m^{-1}$ to >0.35 $kW{\cdot}h{\cdot}m^{-2}{\cdot}\mu m^{-1}$ with the increase of the treatment time, being slightly higher in the case of PEO-S at long treatment time. It is important to note that the coatings formed at 600 s and 900 s for the PEO-S electrolyte show similar energy consumption, which may be associated with the fact that the growth rate of the coating is relatively constant with treatment time. Understandably, that happened in suspension electrolyte where the incorporation of particles from the electrolyte contributes to the formation of a new coating material. These energy consumption values are about the same as the ones reported for low-energy PEO treatments developed for a Mg alloy [17] (~9043.7 $kJ{\cdot}dm^{-2}{\cdot}\mu m$) and lower compared with those previously reported by the Authors for as-cast MgZnCa and Mg3Zn0.4Ca alloys in fluorine electrolyte (1.6 and 1.9 $kW{\cdot}h{\cdot}m^{-2}{\cdot}\mu m^{-1}$, respectively) [7].

3.2. Coating morphologies, structure and composition

Fig. 2 shows the surface and cross-sectional morphologies of PEO-T and PEO-S coatings at different treatment time with their respective EDS analysis (Table 2). As shown in Fig. 2. (a-c, g-i), similar morphologies are observed for all coatings; where the pores are homogeneously distributed on the surfaces of the coatings. In some cases, fine microcracks (Fig. 2 (a, h, i)) are formed due to thermal stress caused by a rapid cooling process [18]; although they are unlikely to be specific to the treatment. According to the surface roughness, the average value of S_a of PEO-T and PEO-S coatings tend to remains constant (~0.7 μm) while that of S_{10z} tends to increase with the treatment time (PEO-T: 9 to 13 μm and PEO—S: 6 to 14 μm, see Table 2). In addition, the density of pores increases with the increase of treatment time for from $4.06{\cdot}10^6$ to $4.17{\cdot}10^6$ pore/mm^2 and from $3.08{\cdot}10^6$ to $4{\cdot}10^6$ pore/mm^2 PEO-T and PEO-S, respectively. The micropore diameters remain constant for PEO-T ~0.25 μm and slightly decrease for PEO-S from 0.32 to 0.25 μm (Table 2), respectively. In most of the PEO/Mg works reported in the literature, the average of pore size increases with increase of the treatment time due to the discharging channels tending to merge leading to contribution to the enlarged pore size [18,19]. The opposite situation is observed here, although the energy consumption is higher with treatment time, as observed in Fig. 1 (b). This may be associated with the lesser intensity of the microdischarges in the main surface area, while most of the energy being involved in the development of a few isolated microarc events [20]. Additionally, the sub-micrometric pores may be due to the gas bubbles passing through the molten oxide material displaced by microarc events.

The cross-sectional morphology of the coatings formed in both electrolytes present a small internal pores and in some cases discharge channels close to the barrier layer are formed (Fig. 2 (d, f, k, l)). The coatings formed in PEO-T appear more compact with only few internal

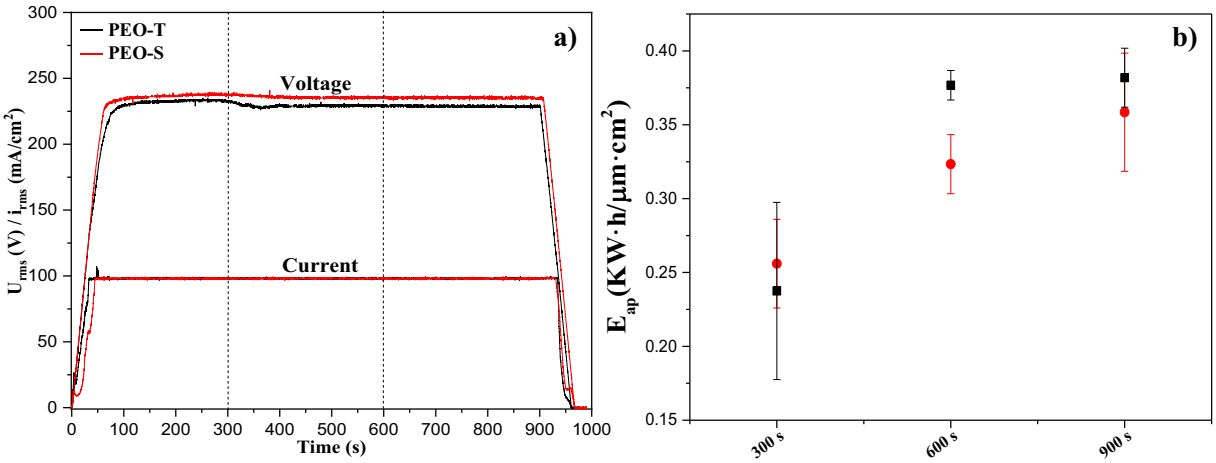

Fig. 1. (a) Current density-time curves and (b) calculated apparent specific energy consumption for PEO-T (black-squares) and PEO-S (red-circles) coatings on Mg3Zn0.4Ca alloys.

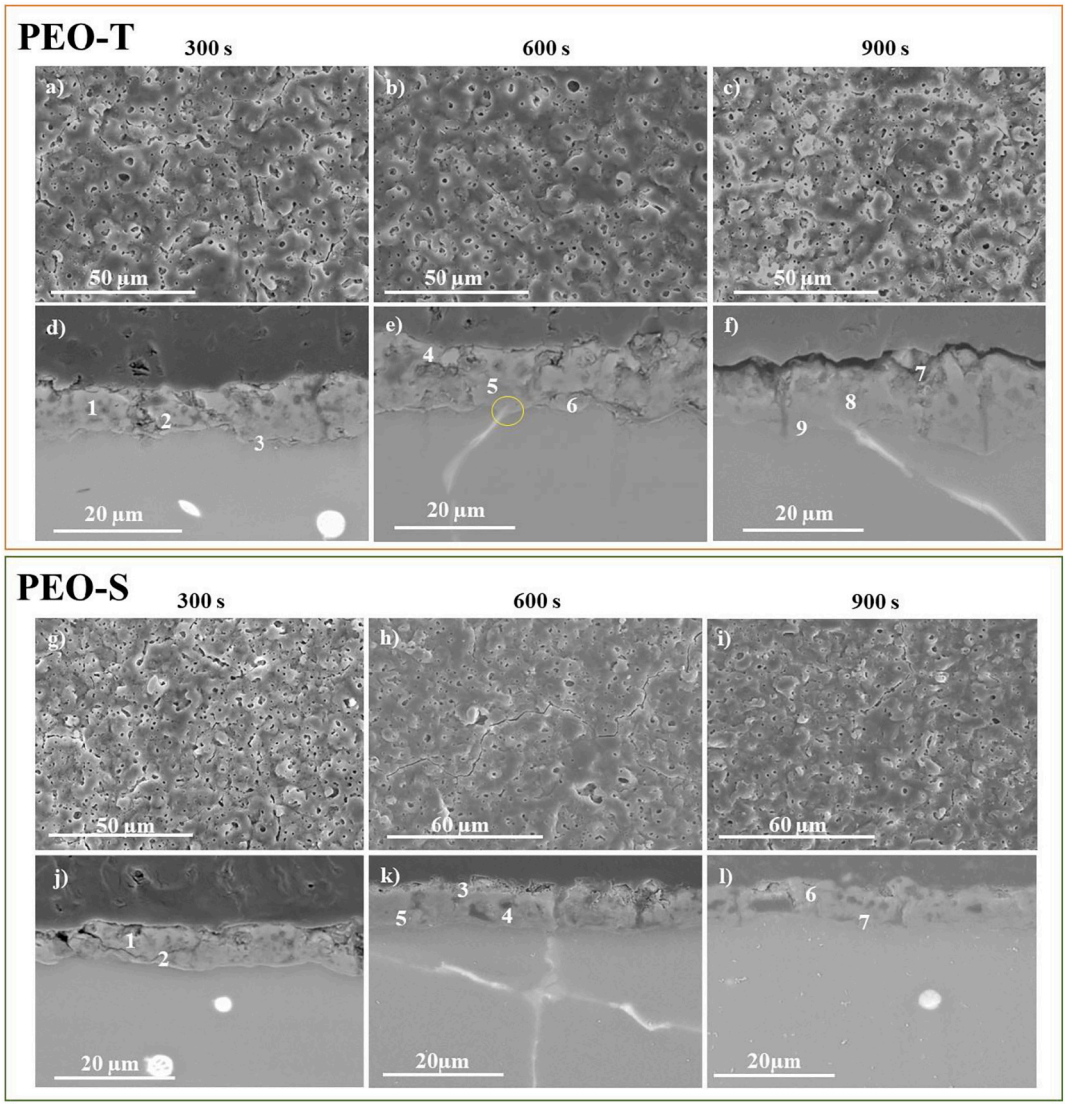

Fig. 2. Secondary electron micrographs of surface (a-c, g-i) and cross-sectional (d-f, j-l) morphology of the (a-f) PEO-T and (g-l) PEO-S coatings produced on Mg3Zn0.4Ca alloys in: 300 s (a, d, g, j), 600 s (b, e, h, k) and 900 s (c, f, i, l).

Table 2
Coatings roughness and surface porosity characteristics.

Parameters	PEO-T			PEO-S		
	300 s	600 s	900 s	300 s	600 s	900 s
S_a (µm)	0.68 ± 0.05	0.71 ± 0.0.7	0.62 ± 0.01	0.51 ± 0.08	0.53 ± 0.10	1.91 ± 0.16
S_{10z} (µm)	9.13 ± 2.95	9.88 ± 3.46	12.98 ± 1.05	5.55 ± 1.71	6.94 ± 0.68	14.50 ± 1.81
Thickness (µm)	5.48 ± 0.94	6.46 ± 2.24	7.33 ± 0.99	8.12 ± 0.46	10.1 ± 0.52	15.1 ± 1.99
Surface pore population density (pore/mm^2)	$4.06{\cdot}10^6$	$4.09{\cdot}10^6$	$4.17{\cdot}10^6$	$3.08{\cdot}10^6$	$3.55{\cdot}10^6$	$3.99{\cdot}10^6$
Pore area fraction (%)	3.05	2.74	2.24	4.74	4.42	1.77
Average pore size (µm)	0.28 ± 0.04	0.24 ± 0.03	0.25 ± 0.1	0.32 ± 0.12	0.28 ± 0.06	0.25 ± 0.01

pores compared to PEO-S electrolyte. It is evident that there is no significant increase in coating thickness (~5.5…7.03 µm) with treatment time for PEO-T, while PEO-S coatings are about two times thicker (Table 2). Greater thickness is expected for coatings formed in suspension electrolytes, due to entrapment of particles in the discharge channels, where they melt, get ionized, migrate under the electric field and get incorporated into the oxide coating matrix [21].

A semiquantitative analysis of the elemental composition of the coating is performed by EDS (Table 3). The incorporation of Ca, P, Si, and Zn remains constant with increasing treatment time. These elements are incorporated in the outer part of the coatings, while Zn is incorporated in the inner part. This is due to inward migration of Ca, Si and P from the electrolyte, while Zn migrates from the substrate outwards. It is worth mentioning that the Ca incorporation decreases with increasing treatment time only for PEO-S electrolyte. In addition, the surface Ca/P ratios in coatings formed in PEO-S electrolyte remains constant with the treatment time around ~0.8. This behaviour could be explained by the development of a few isolated microdischarges of greater intensity (i.e. longer lasting) in the suspension electrolyte with time. As a result, these discharges cause a destructive effect, which is associated with the loss of

Table 3
EDS analysis (at. %) of PEO-T and PEO-S coatings ate 300, 600 and 900 s.

Electrolyte	Time (s)	Location	O	Na	Mg	Si	P	K	Ca	Zn	Ca/P
PEO-T	300	Plan view	55.5	2.6	26.7	7.7	3.4	2.2	1.7	0.1	0.50
		1	53.4	1.2	31.0	9.1	4.6	0.7	1.1	0.1	0.24
		2	48.3	0.3	44.8	3.8	1.9	0.9	0.1	0.3	0.05
		3	33.1	0.2	62.0	2.8	1.3	0.3	0.0	0.5	0.00
	600	Plan view	57.4	1.6	27.1	7.8	3.6	1.0	1.3	0.2	0.36
		4	50.2	1.6	31.9	8.7	4.4	1.4	1.8	0.1	0.41
		5	41.7	0.5	45.9	5.7	3.8	0.7	1.0	0.6	0.26
		6	48.6	0.4	47.9	1.9	0.7	0.3	0.1	0.2	0.14
	900	Plan view	55.6	2.6	26.5	7.6	3.5	2.2	1.7	0.4	0.49
		7	52.9	2.2	30.1	8.2	3.5	1.8	1.1	0.2	0.31
		8	41.2	1.3	37.2	10.4	5.2	2.0	2.0	0.7	0.38
		9	37.1	0.3	56.9	2.9	1.8	0.1	0.1	0.8	0.06
PEO-S	300	Plan view	48.4	1.7	34.1	9.4	2.7	0.7	2.6	0.4	0.96
		1	37.6	0.3	55.7	4.8	0.6	0.0	0.2	0.8	0.33
		2	42.7	2.2	37.0	12.9	2.8	0.9	1.3	0.2	0.46
	600	Plan view	34.0	0.9	49.0	11.3	2.9	0.3	1.6	0.0	0.55
		3	27.0	0.5	64.0	5.6	1.6	0.0	1.3	0.0	0.75
		4	41.8	1.9	39.0	12	2.8	1.0	1.1	0.4	0.39
		5	34.1	0.7	44.7	14.7	4.5	0.2	0.3	0.8	0.07
	900	Plan view	11.4	0.4	80.0	4.7	1.6	0.0	1.0	0.9	0.63
		6	53.7	3.9	29.6	7.8	3.4	0.8	0.8	0.0	0.24
		7	45.8	2.2	34.2	14.1	2.9	0.6	0.1	0.1	0.03

the previously formed material at the site of microdischarges and the formation of new material [22]. In comparison, Ca/P ratios in the surface of the coatings formed in PEO-T electrolyte are inferior by 2 times, but are maintained relatively constant with the increase of the treatment time. This is an indication of milder character of microdischarges that took place in this electrolyte.

The corrosion protection of a PEO coating depends on the corrosion resistance of the barrier layer. Therefore, the PEO-S coating formed in 300 s, as the most compact one (Fig. 2 (j)), has been selected to analyse the barrier layer in more detail. TEM analysis (Fig. 3 (a)) shows a barrier layer of about ~0.6 μm thickness with a complex stratified morphology comprising an upper porous region (~400 nm), separated from the rest of the PEO coating material by a submicron-size pore band, and an inner region (~200 nm) adjacent to the substrate. It is worth mentioning that several finer nanovoid bands are located inside the inner region of the barrier layer (Fig. 3 (b, c)), delimiting the <100 nm-thick strata of the barrier layer.

A curvature of the barrier layer/substrate interface is also seen below

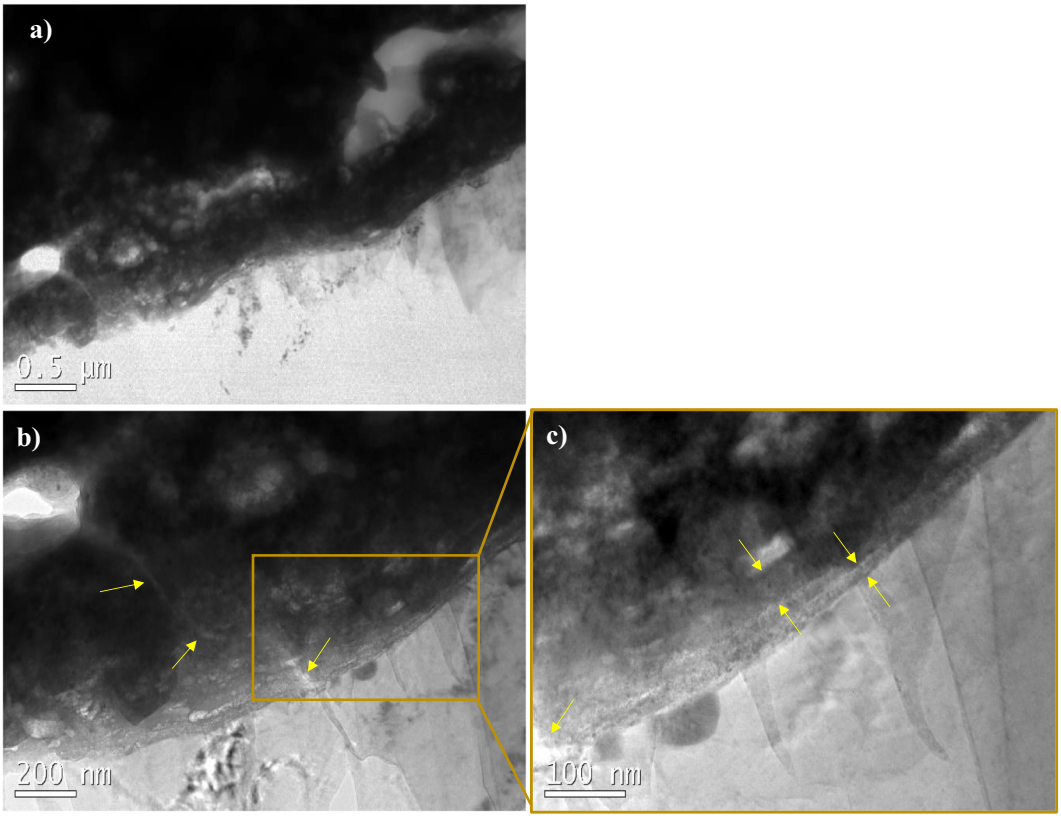

Fig. 3. TEM micrographs of PEO-S coating acquired at 200 kV from different regions of barrier layer. (a) Lower magnifications, (b, c) higher magnifications and (c) detail of barrier layer of Fig. 3 (b).

the pores, which means that the pores represent the bottom of the discharge channels. Fig. 3 (b, c) show discharge channels cutting across almost the entire thickness of the barrier layer. This phenomena is consistent with previous finding of Arrabal on the PEO treated surface of the AZ91-D alloy [23]. It is unclear whether the stratification of the barrier layer is exclusive to AC PEO regime, as no detailed TEM studies of PEO coatings formed in DC mode have been reported so far.

The X-Ray diffraction patterns of all studied coatings are displayed in Fig. 4. All coatings reveal high intensity peaks of Mg (from the substrate), MgO and, in case of PEO-T system, the presence of some amorphous material corresponding to a peak broadening between 25-40° (2θ). In addition, Mg_2SiO_4 (forsterite) is formed in both electrolytes. The silicate species from the electrolyte precipitate as amorphous SiO_2, which reacts with MgO during the microdischarges to form forsterite at the range of 1100–1400 °C [24]. Interestingly, forsterite is present in all PEO-T coatings, but begins to develop in PEO-S only sometime between 300 s and 600 s of treatment (i.e. 300 s coating does not contain Mg_2SiO_4). The crystallinity of the PEO coating is also related to the intensity of the discharge. The higher energy required for coating breakdown and the higher discharge intensity can be observed for longer PEO processing times [18]. This means that a higher temperature is developed in the microdischarges and cooling and solidification take longer, which favours crystallization of Mg_2SiO_4. The absence of Ca- and P-containing crystalline phases in PEO-T and PEO-S coatings suggests that these species are contained in amorphous state. Lack of apatite or hydroxyapatite is understandable, as, typically, greater positive pulse voltage (i.e. greater plasma discharge temperature and slower cooling rate of the material) is required for their formation [19].

3.3. Corrosion behaviour of the coatings

3.3.1. Electrochemical tests

3.3.1.1. Potentiodynamic polarization (PDP). Fig. 5 shows the polarization curves of PEO-T and PEO-S coatings obtained in different treatment times on Mg3Zn0.4Ca alloy after 1 h of immersion in modified α-MEM at 37 °C. The electrochemical parameters calculated from the curves are presented in Table 4.

PEO-T coatings produced a noble E_{corr} shift of 100–200 mV and a 10 times reduction of corrosion current density compared to the bare substrate. It is important to note that the increasing treatment time leads to an increase of i_{corr}, indicating that the coatings become less protective. After E_{corr}, a 200 mV-wide pseudopassivity region is observed in the anodic branches of the curves for all coatings. The E_{pit} is about −1.30 V and is about 120 mV nobler than that of the substrate.

For PEO-S coatings, the E_{corr} is about 70 mV nobler than that for the substrate and the i_{corr} is 20 times lower than that for the substrate for all treatment times. The i_{corr} decreases with treatment time, suggesting that coatings become more protective, although it was observed that with time the coatings develop more internal pores (Fig. 2 (j-l)). The anodic branches disclose behaviour similar to PEO-T, i.e. a pseudopassivity of ~200 mV followed by pitting around −1.35 V. In general, the i_{corr} values of the PEO-S coatings is 2 times lower than for the PEO-T for all treatment times. This suggests that although PEO-S coatings are less compact, they are slightly more protective than PEO-T coatings.

It is worth mentioning that in comparison with the corrosion current data available in the literature for PEO-coated Mg-Zn-Ca systems with alloy compositions similar to the ones of this study, the i_{corr} values obtained in the present work are lower by 2 times. For instance, the PEO process developed on Mg3Zn0.4Ca and Mg1.78Zn0.51Ca alloys yielded i_{corr} of 2.38–7.28 and 5.25 mA/cm^2, respectively [25,26]. This highlights the important influence of the composition of the electrolyte and the parameters of the process on the corrosion performances of the PEO/$MgZn_xCa_y$ systems. However, the PDP results may not necessarily reflect the true ranking of the coating protective capacity, bearing in mind that large polarization is a source of non-stationarity in Mg-based systems. Therefore, an additional screening by EIS appears expedient.

3.3.1.2. Electrochemical impedance spectroscopy (EIS). The screening of PEO-T and PEO-S coatings on Mg3Zn0.4Ca alloy is illustrated in Fig. 6 according to their modulus of total impedance at low frequency ($|Z|_{10mHz}$) after 1 h of immersion in modified α-MEM at 37 °C.

Coating produced in PEO-T electrolyte in 600 s shows considerably better corrosion protection than those formed in 300 and 900 s treatment times. The coatings produced in PEO-S electrolyte in 300 and 600 s, are comparable to each other and to PEO-T-600 s coating, providing the substrate with ~3 times greater corrosion resistance. The 900 s coatings show no significant improvement compared to the substrate.

A detailed analysis of the EIS spectra of all studied coatings, PEO-T and PEO-S, is performed in order to understand the contribution of the coating microstructure and the various electrochemical processes taking place in the coating/substrate systems to their corrosion resistance. Fig. 7 (a, b) shows the Nyquist and Bode plots of the EIS spectra of (a) PEO-T and (b) PEO-S coatings for all treatment times. The respective equivalent circuits and fitting parameters are presented in Fig. 7 (c) and Table 5.

The equivalent circuit used to interpret the EIS results of PEO-T and PEO-S coatings includes R_{el} (solution resistance), R_1/CPE_1 (resistive and

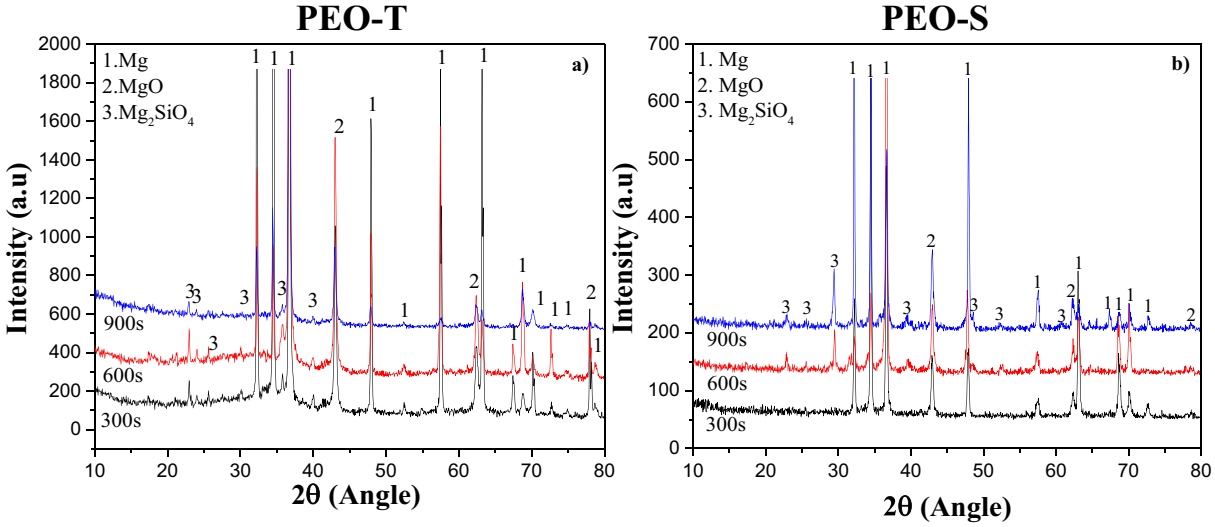

Fig. 4. XRD patterns of (a) PEO-T and (b) PEO-S coatings on Mg3Zn0.4Ca alloy.

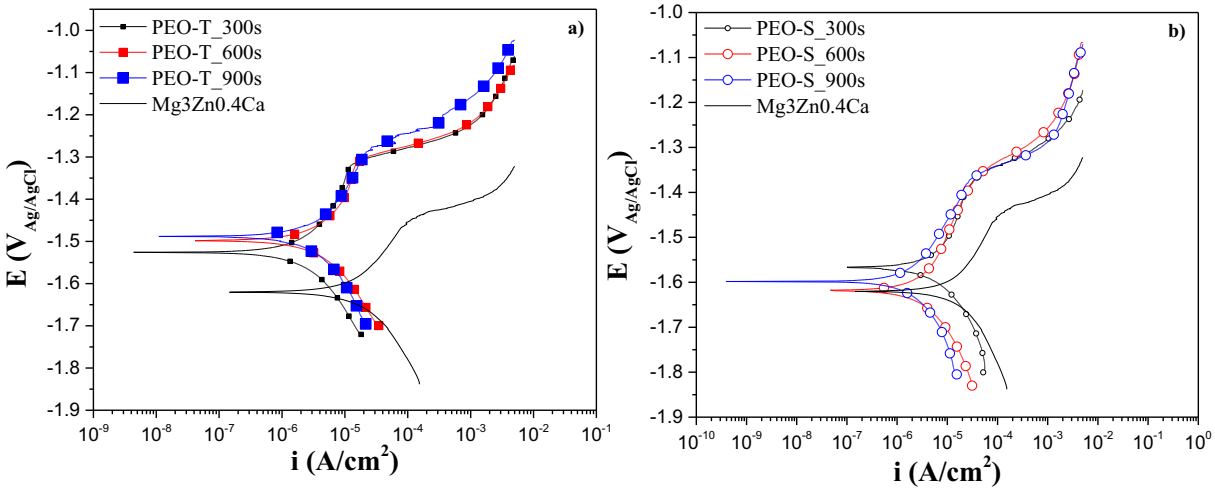

Fig. 5. Polarization curves of (a) PEO-T and (b) PEO-S coatings on Mg3Zn0.4Ca alloy at 300, 600 and 900 s treatment time.

Table 4
Corrosion characteristics from polarization curves from Fig. 5.

Electrolyte	Time (s)	E_{corr} (V)	i_{corr} (μA/cm^2)	E_{pit} (V)
Mg3Zn0.4Ca		–1.62	30.25	–1.42
PEO-T	300	–1.53	2.50	–1.31
	600	–1.50	3.76	–1.30
	900	–1.49	3.02	–1.28
PEO-S	300	–1.57	1.97	–1.36
	600	–1.62	0.99	–1.35
	900	–1.60	0.84	–1.34

capacitive response of the outer-intermediate part of the coatings), R_2/CPE_2 (behaviour of inner barrier layer), and R_{ct}/CPE_{dl} (electrochemical activity at the substrate/electrolyte interface). In the equivalent circuits, the impedance of CPE is calculated by the following equation: $Z = 1/(CPE(j\omega)^n)$; where and j is the imaginary number and $-1 \leq n < 1$. Accordingly, CPE values cited in Table 5 correspond to admittance values at frequency of $\omega = 1$ rad. In case of the substrate, R_1/CPE_1 and R_2/CPE_2 represent the response of Ca-P-rich deposits that form on Mg surface in modified α-MEM and of the corrosion products layer, respectively.

The fitted data of Table 5 indicates that the barrier layer is the main factor responsible for the corrosion protection of the alloy, where R_1 is lower than R_2 for all treatment times and both studied electrolytes. On the one hand, comparing the different treatment times for PEO-T electrolyte, the values of R_2 and R_{ct} are considerably (three or more times) higher for the 600 s coating compared to other treatment times. Furthermore, it is worth noting that the R_2 values for the PEO-T coatings at 300 and 900 s are similar to that of the substrate. This suggests that both coatings are poorly protective and their barrier layer has degraded,

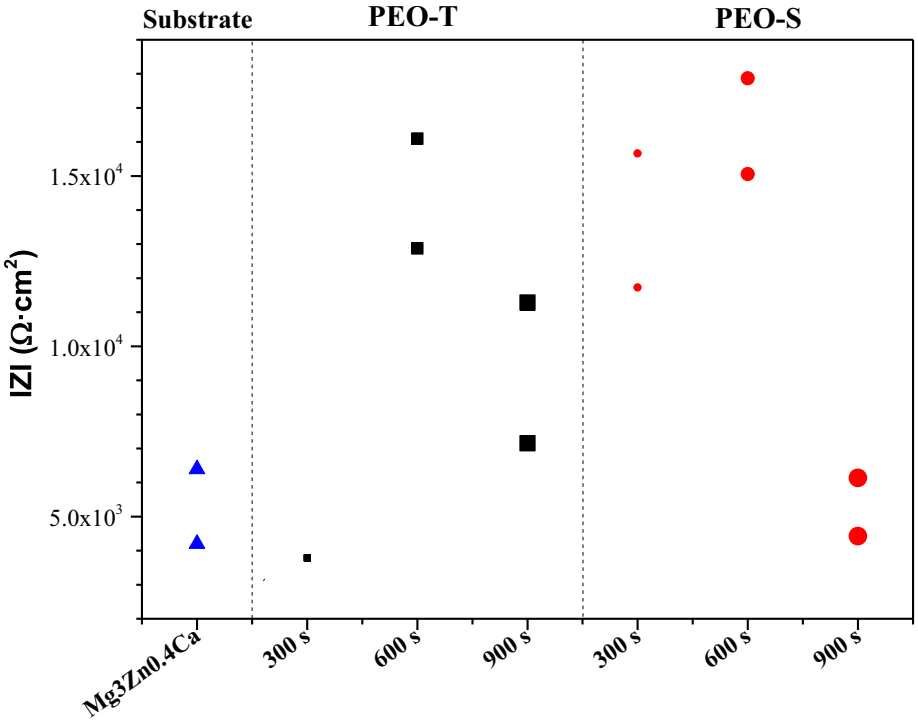

Fig. 6. Scatter diagram of the total impedance modulus values for that substrate and the studied PEO coatings.

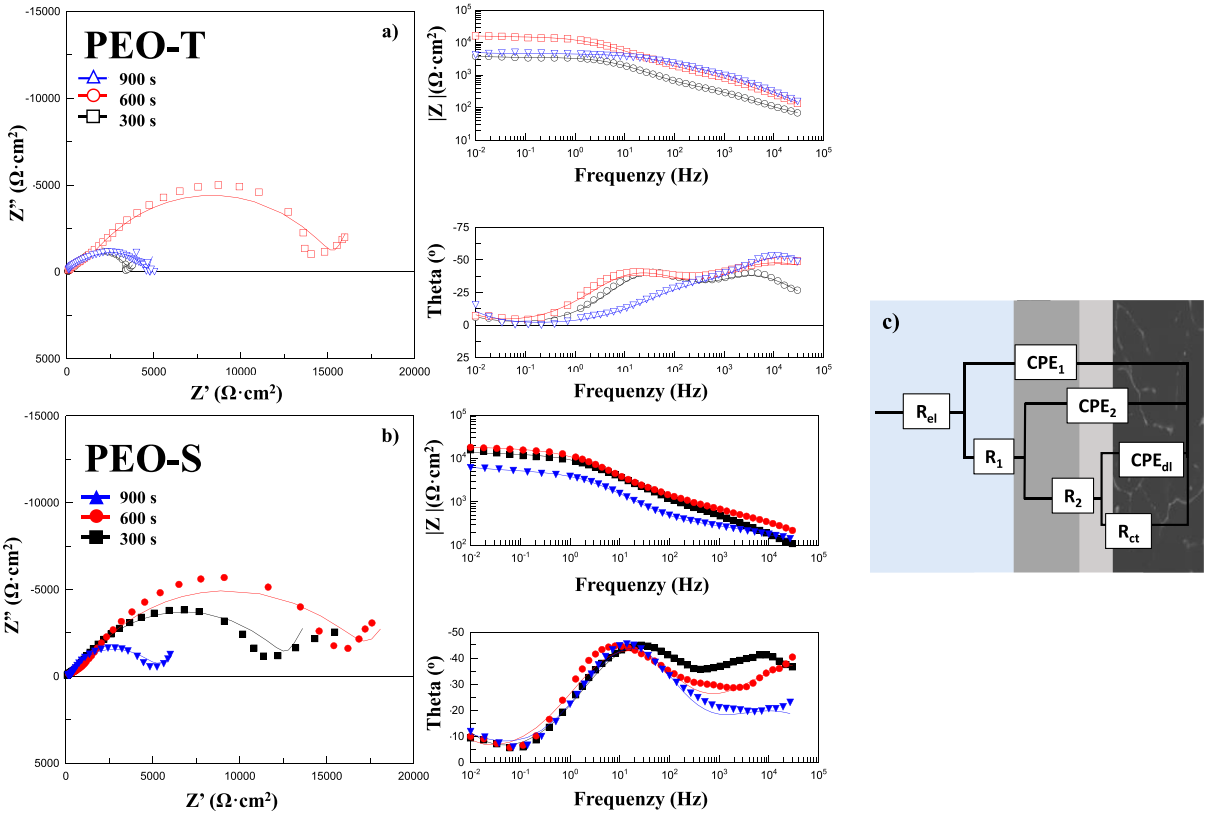

Fig. 7. Nyquist and Bode plots of (a) PEO-T and (b) PEO-S coatings for Mg3Zn0.4Ca alloys after 1 h of immersion in α-MEM solutions at 37 °C. (c) Equivalent circuit used to fit EIS. Symbols - open for PEO-T and filled for-PEO-S coatings and colour associated to treatment time: black −300 s, red −600 s and blue −900 s.

Table 5
Fitted electrical parameters of EIS spectra after 1 h of immersion in inorganic α-MEM solution.

Sample	Time (s)	R_{elec} ($\Omega\cdot cm^2$)	CPE_1 ($\mu S\cdot s^n\cdot cm^{-2}$)	n_1	R_1 ($\Omega\cdot cm^2$)	CPE_2 ($\mu S\cdot s^n\cdot cm^{-2}$)	n_2	R_2 ($\Omega\cdot cm^2$)	CPE_{dl} ($mS\cdot s^n\cdot cm^{-2}$)	n_3	R_{ct} ($\Omega\cdot cm^2$)	R_{total} ($\Omega\cdot cm^2$)
Substrate		56.9	26.6	0.63	198	19.7	0.89	3014	2.1	0.51	3800	7068.9
	300	43.9	7.3	0.67	585.5	11.9	0.78	3002	26.7	0.9	5310.4	8941.8
	600	29.5	2.7	0.66	1762	7.41	0.69	13896	5.78	0.9	32523.5	48211
PEO-T	900	34.1	0.7	0.75	1255	8.6	0.59	3419	12.9	0.9	13408.1	18116.2
	300	36.6	4.8	0.64	839.1	10.4	0.68	12286	4.44	0.9	30760.7	43922.4
	600	21.9	6.0	0.54	1036	10.1	0.69	17130	5.3	0.9	38187.9	56375.8
PEO-S	900	74.7	17.8	0.54	298.8	19.4	0.77	5075	4.3	0.68	12301.5	17750

since it exhibits the same resistance as the corrosion products layer in the substrate. This happens because they are not very compact (note the penetrating transverse microcracks in the 300 s and 900 s coatings in Fig. 2) allowing for easy permeation of corrosive species from the medium.

In case of the suspension electrolyte, the coatings at 300 and 600 s present similar values of R_1 and R_2, being 4–5 times and 2–3 times higher, respectively, compared to the coating at 900 s and the substrate. This fact suggests that both coatings present a high protection due to their compact morphology (few internal pores in cross-sections, Fig. 2) and better state of the barrier layer. The overlapping dispersion of their $|Z|_{10mHz}$ values (Fig. 6) suggests that the difference between the two coatings cannot be considered as statistically significant.

In regards to the slight differences between the two best coatings in each electrolyte system, PEO-T (600 s) and PEO-S (300 s), that showed very similar R_1 and R_2 values, these could possibly be attributed to the greater pore area fraction and slightly bigger internal pore size. This explains the somewhat lower $|Z|_{10mHz}$ values for PEO-S in the intermediate frequencies range.

Comparing the results obtained in PDP and EIS, there is a clear discrepancy in ranking of PEO-T (600 s) and PEO-S (300 s), although the differences in i_{corr} and R_{total} can be considered negligible. Apart from the intrinsic reasons, such as coating characteristics, this may be due to the insufficiently long immersion period (1 h) before EIS measurements [27]. Since PEO-T (600 s) and PEO-S (300 s) coatings have been identified by EIS as nearly identical in terms of their average $|Z|_{10mHz}$ (~14 $k\Omega\cdot cm^2$), for this reason, both coatings are further evaluated by hydrogen evolution measurements in modified α-MEM with CO_2 flow controlled pH during 120 h of immersion, a period which is comparable to the duration of a standard *in vitro* cell proliferation test. This is done in order to i) verify the EIS screening results; ii) discriminate the coatings and determine the realistic degradation rate and iii) examine the development of corrosion products.

3.3.1.3. Hydrogen evolution. PEO-T specimen shows a quick acceleration of corrosion rate after 3 h of immersion (Fig. 8 (a)). This can be related to the loss of the protective properties of the coating due to the penetration of corrosive species through the discharge channels and strata in the barrier layer. After that time, the degradation rate of the coated specimen remained relatively constant (no marked change of the

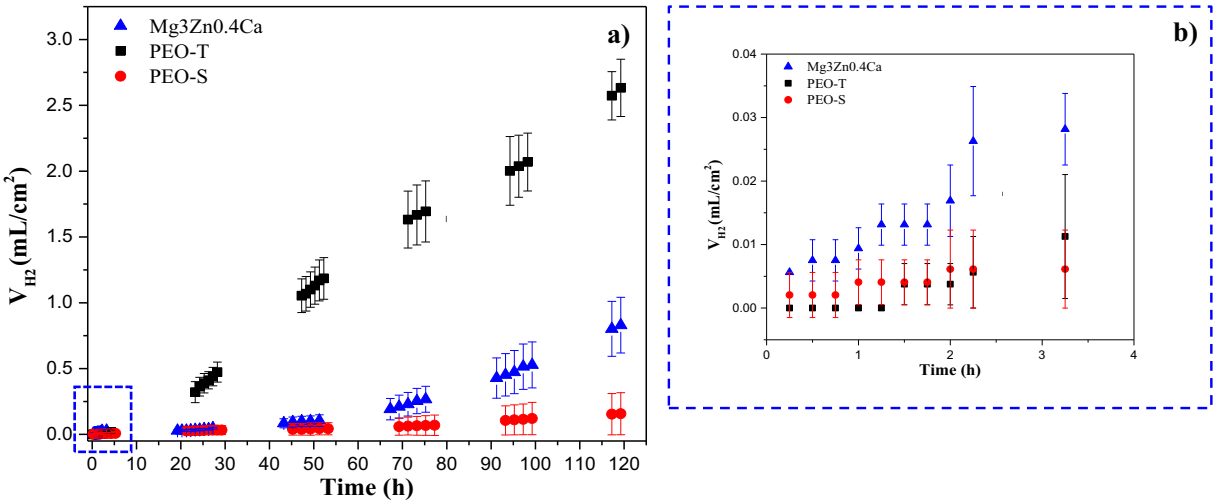

Fig. 8. Hydrogen evolution of PEO-T and PEO-S coatings for the alloy in inorganic α-MEM solution at 37 °C controlling pH at 7.4: (a) for 120 h; (b) amplification for the initial 3 h.

slopes) until the end of the test. Therefore, this specimen exhibits 4 times higher hydrogen volume compared to the substrate which is opposite to the observed in other studies of PEO-treated Mg alloys [28]. It is noteworthy that both coatings were protective and very similar in terms of H_2 volume within firths 3 h of the test (Fig. 8 (b)). The PEO-S coating discloses differing behaviour from that point on; the shallow and relatively constant slope of H_2 evolution curve indicating that the coating maintains its protective effect during the test. After 5 days of immersion, the PEO-S coating showed lower H_2 volume (0.12 mL/cm^2) compared to the substrate (0.88 mL/cm^2) and the PEO-T coating (2.7 mL/cm^2), which is in agreement with the PDP measurements (Fig. 5).

It is worth mentioning that the solubility of H_2 gas in water (1.4 mg/mL at 37°C) leads to the dissolution of the hydrogen generated in 21 L of the solution before the partial pressure becomes sufficient to displace the medium in the burette. Considering this, the plotted data were corrected accordingly, in order to obtain the average degradation rates. The experimentally collected total hydrogen volume has been corrected in order to take into account the amount of the dissolved gas and obtain true degradation rates of the studied specimens at 37 °C (Table 6). Comparing the coatings, it is evident that the coating produced in PEO-S electrolyte offers protection, while the one formed in transparent electrolyte accelerates corrosion of Mg. The possible reason for the high corrosion rate of PEO-T may be due to two factors: (i) the early formation of a crevice at the coating/substrate interface, as seen in previous work [7], and (ii) the formation of ZnO by the oxidation of $Ca_2Mg_6Zn_3$ phase of the alloy. Studies of corrosion of galvanised steel have reported that ZnO in the presence of carbonates (by dissolved CO_2 from the air) forms different corrosion products in the anodic (e.g. $Zn_5(OH)_8Cl_2{\cdot}H_2O$) and cathodic (e.g $Zn_5(OH)_6(CO_3)_2$) areas. These corrosion products may act as semi-permeable membranes, which transport anions (Cl^-) and impede the transport of cations (e.g. H^+), promoting the transport of ionic flows and preserving acidic conditions in the anodic area [29,30], leading to increase of the localised corrosion attack. This behaviour should occur in both coatings since it depends on the oxidation of the same secondary phases of the alloy. However, this is not observed for the PEO-S coating. The possible reasons for that will be discussed further. Clearly, the immersion test results allowed for greater discrimination between the coatings than the EIS or PDP measurements after 1 h of immersion (Figs. 5 and 7), and may be associated with the initiation and extent of localised corrosion that can only be revealed at longer immersion times.

Table 6
Corrected H_2 volume obtained from Fig. 8.

Electrolyte	Time (s)	V_{H2} corrected (mL/cm^2)	Degradation rate (mm/year)
Mg3Zn0.4Ca		2.6 ± 0.7	1.04
PEO-T	600	6.4 ± 3.7	2.57
PEO-S	300	2.5 ± 0.9	0.72

According to the literature, the corrosion performance of PEO/Mg-Zn-Ca systems evaluated by electrochemical or immersion tests reveals that PEO coatings improve the corrosion performance of the substrates [11–16]. In the present work, it was revealed that PEO coatings improved corrosion performance for short-term evaluation (PDP, EIS and H_2 for 3 h) with a superior performance of the coated systems, while long-term immersion tests after 5 days revealed significantly higher degradation in the case of the PEO-T system. Direct comparison of the long-term protective capability of the coatings found in the literature with the present work is difficult due to several different aspects: i) in the immersion tests, the volume of released hydrogen is not measured and, most importantly, a constant pH of the corrosive medium is not maintained during the test; ii) only a visual examination of the corrosion products is performed after the tests, which is not insightful for the determination of the corrosion mechanism.

In order to understand the corrosion behaviour of the coated systems, macro- and micro-morphological examination of the specimens after 5 days of immersion is illustrated in Fig. 9. The coating formed in PEO-S electrolyte do not show any sign of localised corrosion (Fig. 9 (e)), while for PEO-T electrolyte the localised process have already extended severely (Fig. 9 (a)). The detailed cross-sectional examination of PEO-T and PEO-S coatings (Fig. 9 (b, c, f, g)) disclose a thick uniform corrosion products layer in the range of 50–100 μm with the presence of cracks. Remarkably, the hydrated coating is still present over the corrosion products in both coatings. These findings are similar to those regarding the F-containing coatings earlier discussed in Authors' previous work [7]. In comparison with the results of other published works, the onset of corrosion in the present systems is rather early. For instance, for PEO-coated Mg0.8Ca the initiation of the undercoating corrosion product layer was reported after 2 weeks of immersion [31], although the coatings in question were 4 times thicker and contained a high level of fluorine.

The EDS analysis of the corrosion products is presented in Fig. 9 (d, h). Overall, the corrosion product layer in both cases contain elevated levels of Ca and P. Importantly, PEO-T contains significantly more Na, Cl, Ca and P deep in the undercoating corrosion products than PEO-S in a similar location (point 4 and 6–8, respectively). This suggests that PEO-S coating system is much less permeable and possesses better barrier

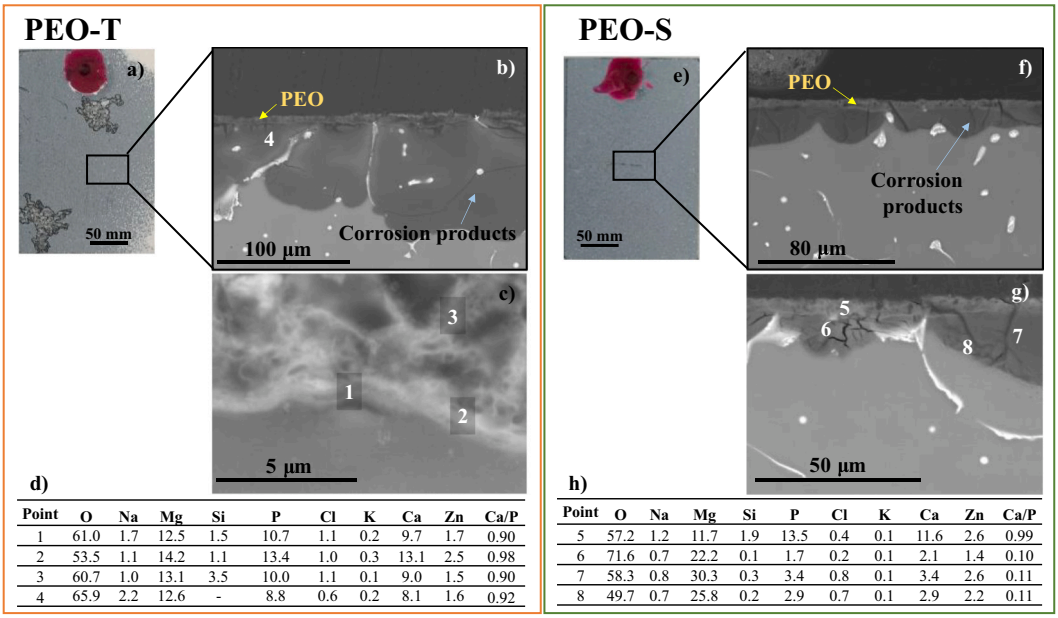

Point	O	Na	Mg	Si	P	Cl	K	Ca	Zn	Ca/P
1	61.0	1.7	12.5	1.5	10.7	1.1	0.2	9.7	1.7	0.90
2	53.5	1.1	14.2	1.1	13.4	1.0	0.3	13.1	2.5	0.98
3	60.7	1.0	13.1	3.5	10.0	1.1	0.1	9.0	1.5	0.90
4	65.9	2.2	12.6	-	8.8	0.6	0.2	8.1	1.6	0.92

Point	O	Na	Mg	Si	P	Cl	K	Ca	Zn	Ca/P
5	57.2	1.2	11.7	1.9	13.5	0.4	0.1	11.6	2.6	0.99
6	71.6	0.7	22.2	0.1	1.7	0.2	0.1	2.1	1.4	0.10
7	58.3	0.8	30.3	0.3	3.4	0.8	0.1	3.4	2.6	0.11
8	49.7	0.7	25.8	0.2	2.9	0.7	0.1	2.9	2.2	0.11

Fig. 9. (a, e) Macrographs and cross-section of (b, c) PEO-T and (f, g) PEO-S coatings for Mg3Zn0.4Ca after 5 days of immersion in modified α-MEM solution. (d, h) EDS analysis (at. %) of PEO-T and PEO-S after H_2 evolution test.

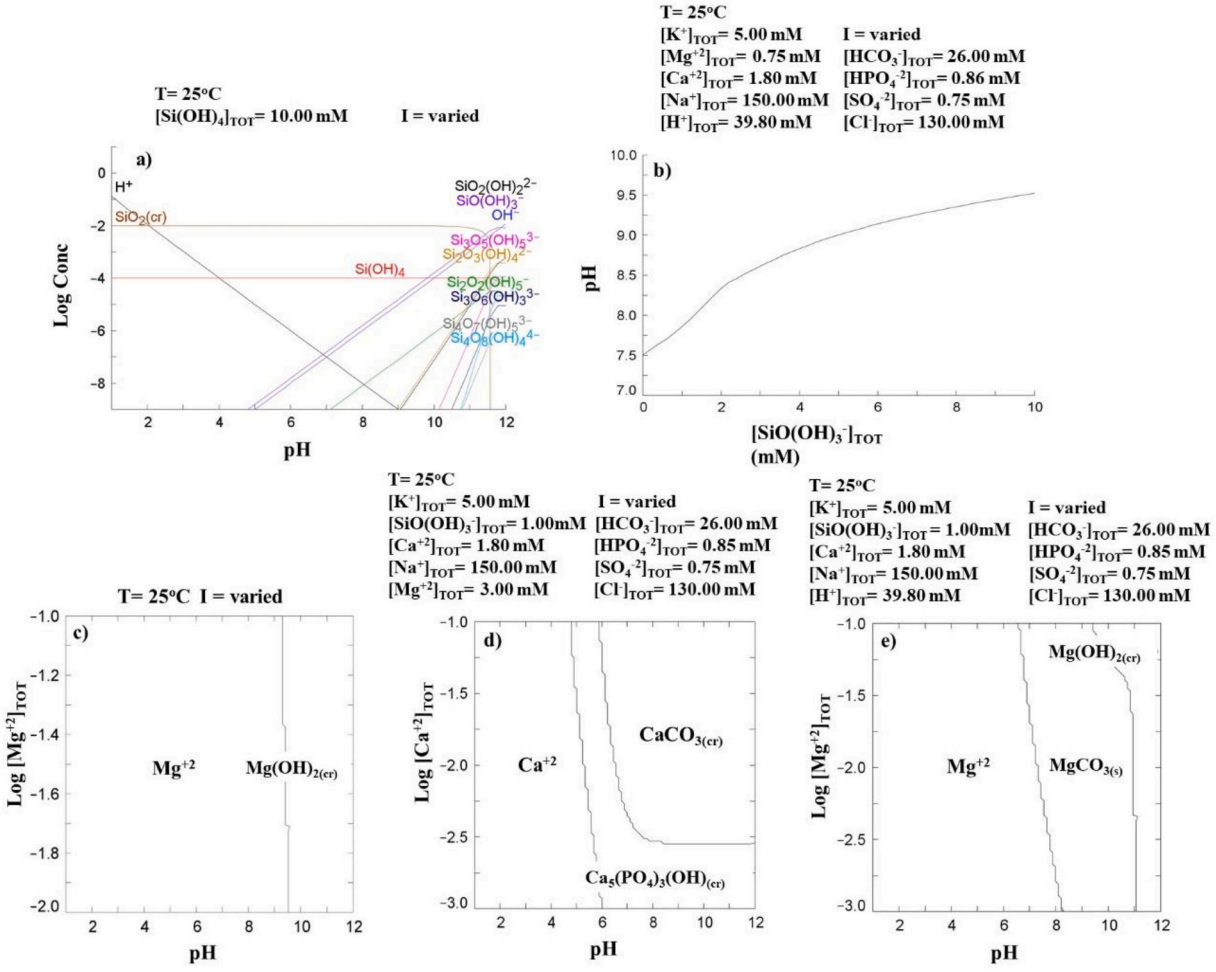

Fig. 10. Equilibrium diagrams for (a) silicate species and (b) modified α-MEM solution in presence of hydrolysed silica species. (c) Solubility diagram for Mg species. Predominance area diagrams for (d) Ca and (e) Mg species in α-MEM.

properties compared to the PEO-T system. The latter may be explained by the fact that silicate species present in PEO-S (300 s) coating are in amorphous state, while in PEO-T (600 s) they form crystalline compound, forsterite. Amorphous silica is soluble in water ($pK_s = 2.76$) in atmospheric conditions [32] while Mg_2SiO_4 is not [33,34]. The dissolution of amorphous silica proceeds as follows:

$$SiO_2 + 2H_2O \leftrightarrow Si(OH)_4 \quad (1)$$

$$Si(OH)_4 + OH^- \leftrightarrow SiO(OH)_3^- + H_2O \quad (2)$$

Reaction (2) is especially facilitated by corrosion of Mg that generates an excess of hydroxyl groups. $Si(OH)_4$ tends to form a gel that is commonly used for purification of water, i.e. it is able to trap inorganic impurities, such as Ca and P species in the present case [35,36] previously, the Authors have shown that silica-reach PEO coatings exhibit self-sealing effect [37]. Equilibrium diagram (constructed using *Spana* free software) for hydrolysis of amorphous silica (Fig. 10 (a)) shows that dissolution of SiO_2 and an increase in deprotonated hydrous silica, $SiO(OH)_3^-$, concentration results in alkalization of the modified α-MEM solution (Fig. 10 (b)). This is consistent with experimentally observed change in pH of the modified α-MEM during corrosion of Mg3Zn0.4Ca alloy with a hybrid coating that comprised a PEO-S layer [38]. More alkaline conditions stabilize the layer of $Mg(OH)_2$ (Fig. 10 (c)) and facilitate precipitation of $MgCO_3$ (Fig. 10 (e)).

It is worth mentioning that the low corrosion rate of PEO-S may also be associated with hydroxyapatite precipitation (Fig. 10 (d)) that remains entrapped and sealed by hydrolysed silica in the pores and cracks case of PEO-S. Ca species are known to adsorb such sealing prevents the access of the corrosive species, whereas in case of PEO-T the diffusion of Ca, P, Na and Cl species is much less hindered. This is consistent with the slightly lower amount of Ca and P (~2 %, point 6, Fig. 9 (g)) in the corrosion products for PEO-S coating than for PEO-T (~9 and ~ 10 at. %, point 4, Fig. 9 (b)). Note, that the Ca and P content in the still attached portion of PEO-S (300 s) post immersion is up to ~4 times greater than in the as-received coating (3.8 and 2.8 at. %). The discussed above is in agreement with several works that have reported $Mg(OH)_2$, $Ca_{10}(PO_4)_6(OH)_2$, $(Ca,Mg)_3(PO_4)_2$, $Mg(HCO_3)(OH)\cdot 2H_2O$ or $MgCO_3\cdot 3H_2O$ as the main corrosion products formed on Mg-Zn-Ca alloys [11,13,39].

Additionally, Zn is found both in inner and outer part of the corrosion products (e.g. points 4, 6; Fig. 9 (b, g)) due to the diffusion of Zn from the bulk material. It may participate in formation of amorphous ZnO, $ZnPO_4$, $ZnCO_3$, and/or $Zn(OH)_2$ [28,29]. Ca/P ratio in the attached parts of the coatings and the corrosion products is elevated and ranged from 0.1 to 1, and are mostly non-stoichiometric with respect to 1.5 or 1.67 ratio of apatite and hydroxyapatite. Elevated content and lixiviation of Ca and P are expected to contribute to the growth of the bone, improving the biocompatibility of the implant in the human body [40,41].

Several important factors corresponding to the corrosion mechanisms are illustrated by post-corrosion characterization: a) the coatings appeared well adhered after 5 days of immersion; b) the presence of cracks is evident in the corrosion products layer and c) a few Zn-rich intermetallics are embedded into the corrosion products. According to this, the degradation of both PEO-coated Mg3Zn0.4Ca alloy in modified α-MEM proceeds in accordance with the following mechanism: i) the corrosive species from the media penetrate through the microdefects in the outer porous layer, leading to progressive hydration of the coating and degradation of the inner barrier layer. ii) The corrosion products react with the species from the media leading to the precipitation of Ca—P based compounds which inhibit the degradation of the alloy; iii) the coating prevents the detachment of the corrosion product layer, resulting in fewer cracks and trapped or undissolved intermetallics. iv) The Zn- and impurity-rich intermetallics that oxidize very slowly form galvanic couples with the matrix, and accelerate the corrosion process of the adjacent matrix grains. v) The cracked undercoating corrosion products layer is a crevice between the adhered PEO coating and the substrate [7], and the formation of ZnO from the oxidation of secondary phases, accelerated the corrosion rate of the PEO-coated system.

3.4. Conclusions

- Ca-P-Si-containing coatings were developed at different treatment times in transparent and suspended electrolytes on Mg3Zn0.4Ca alloy.
- Slightly higher energy consumption was obtained with the increase of the treatment time, being slightly higher in the case of PEO-S electrolyte at longer treatment times.
- Coatings formed in suspended electrolyte are two times thicker and more compact compared to PEO-T electrolyte. All systems mainly consisted of MgO and Mg_2SiO_4 phases with some Ca—P amorphous-containing phases.
- Short-term electrochemical evaluation (EIS and PDP) revealed controversial results due to the limitation of those methods for Mg alloys. Namely, while PDP tests confirmed that all coatings developed in fluorine-free electrolytes can offer corrosion protection, EIS measurements demonstrated that only PEO-T (600 s) and PEO-S (300 and 600 s) enhanced the substrate corrosion protection.
- Short-term H_2 evolution measurements revealed protective properties for all the selected PEO coatings. At longer immersion times (5 days), only PEO-S coating showed improved corrosion performance compared to the bulk material, i.e., the PEO-S coating showed twice lower corrosion rate (0.7 mm/yr) compared to PEO-T coating and substrate (2.5 and 1.0 mm/yr, respectively). This could be associated with the precipitation of hydroxyapatite that remains trapped in the pores and cracks of the PEO by the solubilisation and hydrolysis of amorphous SiO_2 from the PEO in water.
- The lower corrosion performance of PEO-T coating was mainly due to (i) the permeability of the PEO coating and (ii) the presence of discharge channels in the barrier layer, thus facilitating the access of corrosive species. As a consequence, the superior degradation rate of the PEO-T coating compared to PEO-S coatings was associated with the formation of crevices at the PEO/substrate interface and the oxidation of $Ca_2Mg_6Zn_3$ to ZnO, thus favouring localised corrosion phenomena.

Declaration of competing interest

The authors declare that they have no known competing financial interests or personal relationships that could have appeared to influence the work reported in this paper.

Data availability

The raw/processed data required to reproduce these findings cannot be shared at this time as the data also forms part of an ongoing study.

Acknowledgements

The authors gratefully acknowledge the support of [PID2021-124341OB-C22, MCIU/AEI/FEDER, UE] and ADITIMAT-CM [S2018/NMT-4411, Regional Government of Madrid and EUStructural Funds]. M. Mohedano is grateful for the support of [RYC-2017-21843, Ministerio de Ciencia e Innovación].

References

[1] A. Fattah-alhosseini, R. Chaharmahali, K. Babaei, Impressive strides in amelioration of corrosion and wear behaviors of Mg alloys using applied polymer coatings on PEO porous coatings: a review, J. Magnes. Alloys. 10 (2022) 1171–1190, https://doi.org/10.1016/j.jma.2022.01.015.
[2] A. Fattah-alhosseini, R. Chaharmahali, K. Babaei, M. Nouri, M.K. Keshavarz, M. Kaseem, A review of effective strides in amelioration of the biocompatibility of

PEO coatings on Mg alloys, J. Magnes. Alloys. 10 (2022) 2354–2383, https://doi.org/10.1016/j.jma.2022.09.002.
[3] A. Fattah-alhosseini, M. Molaei, M. Nouri, K. Babaei, Antibacterial activity of bioceramic coatings on Mg and its alloys created by plasma electrolytic oxidation (PEO): a review, J. Magnes. Alloys. 10 (2022) 81–96, https://doi.org/10.1016/j.jma.2021.05.020.
[4] T. Zehra, A. Fattah-alhosseini, M. Kaseem, Surface properties of plasma electrolytic oxidation coating modified by polymeric materials: a review, Prog. Org. Coat. 171 (2022), 107053, https://doi.org/10.1016/j.porgcoat.2022.107053.
[5] H. Mozafarnia, A. Fattah-Alhosseini, R. Chaharmahali, M. Nouri, M.K. Keshavarz, M. Kaseem, Corrosion, Wear, and Antibacterial Behaviors of Hydroxyapatite/MgO Composite PEO Coatings on AZ31 Mg Alloy by Incorporation of TiO2 Nanoparticles, Coatings 12 (2022) 1967, https://doi.org/10.3390/coatings12121967.
[6] T.S.N. Sankara Narayanan, I.S. Park, M.H. Lee, Strategies to improve the corrosion resistance of microarc oxidation (MAO) coated magnesium alloys for degradable implants: prospects and challenges, Prog. Mater. Sci. 60 (2014) 1–71, https://doi.org/10.1016/j.pmatsci.2013.08.002.
[7] L. Moreno, M. Mohedano, R. Arrabal, E. Matykina, Development and screening of (Ca-P-Si-F)-PEO coatings for biodegradability control of Mg-Zn-Ca alloys, J. Magnes. Alloys. (2022), https://doi.org/10.1016/j.jma.2021.12.011.
[8] P. Jiang, R. Hou, S. Zhu, S. Guan, A robust calcium carbonate (CaCO3) coating on biomedical MgZnCa alloy for promising corrosion protection, Corros. Sci. 198 (2022), 110124, https://doi.org/10.1016/j.corsci.2022.110124.
[9] A.R. Rafieerad, M.R. Ashra, R. Mahmoodian, A.R. Bushroa, Surface characterization and corrosion behavior of calcium phosphate-base composite layer on titanium and its alloys via plasma electrolytic oxidation: a review paper, Mater. Sci. Eng. C 57 (2015) 397–413, https://doi.org/10.1016/j.msec.2015.07.058.
[10] O.P. Terleeva, A.I. Slonova, I.V. Mironov, A.B. Rogov, Yu.P. Sharkeev, Microplasma synthesis of biocompatible coatings with additions of magnesium, silicon and silver on pure titanium from homogeneous electrolytes, Surf. Coat. Technol. 307 (2016) 1265–1273, https://doi.org/10.1016/j.surfcoat.2016.05.045.
[11] X. Ly, S. Yang, T. Nguyen, Effect of equal channel angular pressing as the pretreatment on microstructure and corrosion behavior of micro-arc oxidation (MAO) composite coating on biodegradable Mg-Zn-Ca alloy, Surf. Coat. Technol. 395 (2020), 125923, https://doi.org/10.1016/j.surfcoat.2020.125923.
[12] J. Dou, G. Gu, C. Chen, Y. Pan, Characterization and biodegradation behavior of micro-arc oxidation coatings formed on Mg–Zn–Ca alloys in two different electrolytes, RSC Adv. 6 (2016) 104808–104818, https://doi.org/10.1039/C6RA22666C.
[13] N. Zhang, D. Zhao, N. Liu, Y. Wu, J. Yang, Y. Wang, H. Xie, Y. Ji, C. Zhou, J. Zhuang, Y. Wang, J. Yan, Assessment of the degradation rates and effectiveness of different coated Mg-Zn-Ca alloy scaffolds for in vivo repair of critical-size bone defects, J. Mater. Sci. Mater. Med. 29 (2018) 138, https://doi.org/10.1007/s10856-018-6145-2.
[14] J. Dou, Y. Chen, Y. Chi, H. Li, G. Gu, C. Chen, Preparation and characterization of a calcium–phosphate–silicon coating on a Mg–Zn–Ca alloy via two-step micro-arc oxidation, Phys. Chem. Chem. Phys. 19 (2017) 15110–15119, https://doi.org/10.1039/C7CP02672B.
[15] Y. Pan, C. Chen, D. Wang, D. Huang, Dissolution and precipitation behaviors of silicon-containing ceramic coating on Mg–Zn–Ca alloy in simulated body fluid, Colloids Surf. B Biointerfaces 122 (2014) 746–751, https://doi.org/10.1016/j.colsurfb.2014.08.012.
[16] J.H. Gao, X.Y. Shi, B. Yang, S.S. Hou, E.C. Meng, F.X. Guan, S.K. Guan, Fabrication and characterization of bioactive composite coatings on Mg–Zn–Ca alloy by MAO/sol–gel, J. Mater. Sci. Mater. Med. 22 (2011) 1681–1687, https://doi.org/10.1007/s10856-011-4349-9.
[17] Y. Zhang, C. Chen, H. Tian, S. Wang, C. Wen, F. Chen, An ionic liquid-assisted strategy for enhanced anticorrosion of low-energy PEO coatings on magnesium–lithium alloy, J. Magnes. Alloys. (2023), https://doi.org/10.1016/j.jma.2023.01.004.
[18] R. Chaharmahali, A. Fattah-alhosseini, K. Babaei, Surface characterization and corrosion behavior of calcium phosphate (Ca-P) base composite layer on Mg and its alloys using plasma electrolytic oxidation (PEO): a review, J. Magnes. Alloys. (2020), https://doi.org/10.1016/j.jma.2020.07.004.
[19] H. Tang, Y. Han, T. Wu, W. Tao, X. Jian, Y. Wu, F. Xu, Synthesis and properties of hydroxyapatite-containing coating on AZ31 magnesium alloy by micro-arc oxidation, Appl. Surf. Sci. 400 (2017) 391–404, https://doi.org/10.1016/j.apsusc.2016.12.216.
[20] R. Hussein, D. Northwood, Production of Anti-Corrosion Coatings on Light Alloys (Al, Mg, Ti) by Plasma-Electrolytic Oxidation (PEO), 2014, pp. 201–239. Chapter 11.
[21] X. Lu, M. Mohedano, C. Blawert, E. Matykina, R. Arrabal, K.U. Kainer, M. L. Zheludkevich, Plasma electrolytic oxidation coatings with particle additions – a review, Surf. Coat. Technol. 307 (2016) 1165–1182, https://doi.org/10.1016/j.surfcoat.2016.08.055.
[22] X.-N. Gu, Y.-F. Zheng, A review on magnesium alloys as biodegradable materials, Front Mater Sci China 4 (2010) 111–115, https://doi.org/10.1007/s11706-010-0024-1.
[23] R. Arrabal, E. Matykina, T. Hashimoto, P. Skeldon, G.E. Thompson, Characterization of AC PEO coatings on magnesium alloys, Surf. Coat. Technol. 203 (2009) 2207–2220, https://doi.org/10.1016/j.surfcoat.2009.02.011.
[24] G.W. Brindley, R. Hayami, Kinetics and mechanism of formation of forsterite (Mg2SiO4) by solid state reaction of MgO and SiO2, Philos. Mag. J. Theor. Exp. Appl. Phys. 12 (1965) 505–514, https://doi.org/10.1080/14786436508218896.
[25] Y. Wang, M. Chen, Y. Zhao, Preparation and Corrosion Resistance of Microarc Oxidation-Coated Biomedical Mg–Zn–Ca Alloy in the Silicon–Phosphorus-mixed Electrolyte, ACS Omega 4 (2019) 20937–20947, https://doi.org/10.1021/acsomega.9b01998.
[26] J. Dou, J. Wang, Y. Lu, C. Chen, H. Yu, R.L.-W. Ma, Bioactive MAO/CS composite coatings on Mg-Zn-Ca alloy for orthopedic applications, Prog. Org. Coat. 152 (2021), 106112, https://doi.org/10.1016/j.porgcoat.2020.106112.
[27] S. Jr, Electrochemical impedance spectroscopy for the measurement of the corrosion rate of magnesium alloys: brief review and challenges, Metals 10 (2020) 775, https://doi.org/10.3390/met10060775.
[28] D. Liu, G. Xu, S.S. Jamali, Y. Zhao, M. Chen, T. Jurak, Fabrication of biodegradable HA/Mg-Zn-Ca composites and the impact of heterogeneous microstructure on mechanical properties, in vitro degradation and cytocompatibility, Bioelectrochemistry 129 (2019) 106–115, https://doi.org/10.1016/j.bioelechem.2019.05.001.
[29] D. Persson, D. Thierry, O. Karlsson, Corrosion and corrosion products of hot dipped galvanized steel during long term atmospheric exposure at different sites worldwide, Corros. Sci. 126 (2017) 152–165, https://doi.org/10.1016/j.corsci.2017.06.025.
[30] S.M. Manhabosco, M. Taise, N. Manhabosco, V. Geoffroy, L.F.P. Dick Vignal, Corrosion behaviour of galvanized steel studied by electrochemical microprobes applied on low-angle cross sections, Corros. Sci. 140 (2018) 379–387, https://doi.org/10.1016/j.corsci.2018.05.026.
[31] M. Mohedano, B.J.C. Luthringer, B. Mingo, F. Feyerabend, R. Arrabal, P.J. Sanchez-Egido, C. Blawert, R. Willumeit-Römer, M.L. Zheludkevich, E. Matykina, Bioactive plasma electrolytic oxidation coatings on Mg-Ca alloy to control degradation behaviour, Surf. Coat. Technol. 315 (2017) 454–467, https://doi.org/10.1016/j.surfcoat.2017.02.050.
[32] I. Gunnarsson, S. Arnórsson, Amorphous silica solubility and the thermodynamic properties of H4SiO°4 in the range of 0° to 350°C at Psat, Geochim. Cosmochim. Acta 64 (2000) 2295–2307, https://doi.org/10.1016/S0016-7037(99)00426-3.
[33] C.A. Macris, R.C. Newton, J. Wykes, R. Pan, C.E. Manning, Diopside, enstatite and forsterite solubilities in H2O and H2O-NaCl solutions at lower crustal and upper mantle conditions, Geochim. Cosmochim. Acta 279 (2020) 119–142, https://doi.org/10.1016/j.gca.2020.03.035.
[34] S. Demouchy, S. Mackwell, Water diffusion in synthetic iron-free forsterite, Phys. Chem. Miner. 30 (2003) 486–494, https://doi.org/10.1007/s00269-003-0342-2.
[35] K. Szymanek, R. Charmas, W. Piasecki, Investigations of mechanism of Ca2+ adsorption on silica and alumina based on Ca-ISE monitoring, potentiometric titration, electrokinetic measurements and surface complexation modeling, Adsorption 27 (2021) 105–115, https://doi.org/10.1007/s10450-020-00280-x.
[36] K. P's, Treatment of natural surface waters using new composite flocculants-coagulants, Int. J. Hydrol. 4 (2020) 211–217, https://doi.org/10.15406/ijh.2020.04.00248.
[37] E. Wierzbicka, B. Vaghefinazari, S.V. Lamaka, M.L. Zheludkevich, M. Mohedano, L. Moreno, P. Visser, A. Rodriguez, J. Velasco, R. Arrabal, E. Matykina, Flash-PEO as an alternative to chromate conversion coatings for corrosion protection of Mg alloy, Corros. Sci. 180 (2021), 109189, https://doi.org/10.1016/j.corsci.2020.109189.
[38] L. Moreno, C. Wang, S.V. Lamaka, M.L. Zheludkevich, J. Rodríguez-Hernández, R. Arrabal, E. Matykina, Ciprofloxacin release and corrosion behaviour of a hybrid PEO/PCL coating on Mg3Zn0.4Ca alloy, J. Funct. Biomater. 14 (2023) 65, https://doi.org/10.3390/jfb14020065.
[39] J. Dou, Y. Zhao, L. Lu, G. Gu, H. Yu, C. Chen, Effect of the second-step voltages on the structural and corrosion properties of silicon–calcium–phosphate (Si–CaP) coatings on Mg–Zn–Ca alloy, R. Soc. Open Sci. 5 (2018), 172410, https://doi.org/10.1098/rsos.172410.
[40] S. Virtanen, Biodegradable Mg and Mg alloys: corrosion and biocompatibility, Mater. Sci. Eng. B 176 (2011) 1600–1608, https://doi.org/10.1016/j.mseb.2011.05.028.
[41] A.S. Gnedenkov, S.V. Lamaka, S.L. Sinebryukhov, D.V. Mashtalyar, V.S. Egorkin, I. M. Imshinetskiy, M.L. Zheludkevich, S.V. Gnedenkov, Control of the Mg alloy biodegradation via PEO and polymer-containing coatings, Corros. Sci. 182 (2021), 109254, https://doi.org/10.1016/j.corsci.2021.109254.